Coarse-grained Modeling and Dynamics Tracking of Nanoparticles diffusion in Human Gut Mucus

Liming Zhao[1†], Sandra L. Arias[2†], Warren Zipfel[2], Ilana L. Brito[2*], Jingjie Yeo[1*]

† Contributed Equally
* Corresponding authors: Email: ibrito@cornell.edu; jingjieyeo@cornell.edu
[1] Sibley School of Mechanical and Aerospace Engineering, Cornell University, Ithaca, New York, USA
[2] Meinig School of Biomedical Engineering, Cornell University, Ithaca, New York, USA

Abstract:

The gastrointestinal (GI) tract's mucus layer serves as a critical barrier and a mediator in drug nanoparticle delivery. The mucus layer's diverse molecular structures and spatial complexity complicates the mechanistic study of the diffusion dynamics of particulate materials. In response, we developed a bi-component coarse-grained mucus model, specifically tailored for the colorectal cancer environment, that contained the two most abundant glycoproteins in GI mucus: Muc2 and Muc5AC. This model demonstrated the effects of molecular composition and concentration on mucus pore size, a key determinant in the permeability of nanoparticles. Using this computational model, we investigated the diffusion rate of polyethylene glycol (PEG) coated nanoparticles, a widely used muco-penetrating nanoparticle. We validated our model with experimentally characterized mucus pore sizes and the diffusional coefficients of PEG-coated nanoparticles in the mucus collected from cultured human colorectal goblet cells. Machine learning fingerprints were then employed to provide a mechanistic understanding of nanoparticle diffusional behavior. We found that larger nanoparticles tended to be trapped in mucus over longer durations but exhibited more ballistic diffusion over shorter time spans. Through these discoveries, our model provides a promising platform to study pharmacokinetics in the GI mucus layer.

Introduction:

In recent years, designing oral drug nanoparticles has gained increasing interest in pharmaceutics because they can facilitate the bioavailability and therapeutic efficacy.[1] However, a significant obstacle that weakens the drug delivery efficiency is the mucus layer lining the human gastrointestinal (GI) tract, which is primarily composed of water and mucin glycoproteins and other minor molecules such as electrolytes, lipids, and nucleic acids.[2–4] This viscous and dynamic barrier not only plays a crucial role in lubricating and protecting the epithelium from exposure to luminal contents, but also significantly hinders the penetration and absorption of nanoparticle-based drugs.[5–7] The periodic clearance of the mucus layer will remove the trapped drug nanoparticles, limiting their availability at designated target sites.[4,8] Thus, characterizing the mucus's structural and mechanical properties becomes crucial to comprehend how the diffusion of drugs is hindered or facilitated through the mucus. This understanding is pivotal for improving pharmacokinetic predictions related to nanoparticles (NPs) and nanocarriers in treating gastrointestinal diseases and other conditions.

However, due to the molecular diversity and spatial complexity of the GI mucus layer, predicting the interaction and movement of NPs through its layers poses several challenges for pharmacokinetic studies.[9–11] The main building blocks of intestinal mucus, mucin glycoproteins, have a high molecular weight of between hundred thousands to millions of Daltons and contain segments with distinct chemical properties: its protein backbone is partitioned as hydrophobic N-terminal and C-terminal, hydrophobic cysteine domains, and glycosylated regions in the middle.[5,12] Such chemical heterogeneity enables the glycoprotein molecules to interact with both hydrophobic and hydrophilic drugs.[13] Glycoproteins also exhibit remarkable diversity in their molecular structure and functional properties. Mucin glycoproteins are broadly categorized into membrane-associated mucins, such as Muc1, Muc3, Muc20, and secretory mucins, such as Muc2, Muc5AC, Muc5B, and Muc6.[14,15] Different locations in the GI tract or different diseases will alter the compositions of these glycoprotein molecules.[16,17] For instance, the production of Muc2, Muc3, Muc12, Muc13, and Muc17 predominantly occurs in the intestine, whereas Muc5AC and

Muc6 are primarily synthesized in the stomach.[17] Muc2 is secreted within the intestinal tract by goblet cells in healthy individuals[18,19], while during inflammatory bowel disease and colorectal cancer, epithelial goblet cells express Muc5AC and Muc5B, in addition to Muc2.[20–22] Muc5 has different cysteine domain patterns in the PTS region compared to Muc2[16], and cysteine domains significantly affect the polymeric crosslinking and the assembly of the mucus network.[23,24] Therefore, studying a single type of mucin is insufficient to characterize the mucus, especially in regions with lesions that require drug release.

In addition, the diffusion of nanoparticles through the mucus layer is strongly influenced by the characteristics of the nanoparticles, including size, shape, and surface chemistry.[1] Particle size plays a critical role in determining the diffusion rate of nanoparticles through the mucus, the effect of which is tightly related to the mucus pore size.[25,26] The shape of nanoparticles also influences their mucosal transport, with rod-like nanoparticles showing faster penetration ability compared with spherical nanoparticles.[27] Moreover, surface charge and hydrophobicity/hydrophilicity is another critical factor. The presence of hydrophilic polymers and nearly neutral surface, such as polyethylene glycol (PEG) coated nanoparticles, can create a hydration shell that repels the mucin fibers, thereby minimizing adhesive interactions and enhancing muco-penetration.[28–30] In contrast, hydrophobic or highly charged nanoparticles may have higher interactions with the non-polar or polar domains of mucins, respectively, which is in favor of muco-adhesive ability.[25,31,32]

The diversity and complexity of mucus and nanoparticles mentioned above pose design challenges for drug development. Therefore, the development of computational models is indispensable for conducting detailed mechanistic studies on interactions between mucus and particulate materials. Due to the large size of the mucus network, studying the diffusion dynamics of nanoparticles in mucus requires establishing a coarse-grained (CG) model in the mesoscale. However, research on building CG models of mucus communities is relatively few. In 2010, Gniewek and Kolinsk proposed a Monte Carlo scheme to simulate CG mucus.[33] In their model, mucins are constructed by 20 beads, which are classified into three types. The values of repulsive, attractive, and neutral contact potentials were simply set to 0.5, -0.5, and 0. Later, Lísal *et al.* developed a dissipative particle dynamics (DPD) model for studying mucin aggregation,

which used a better physical model to describe the hydrophobicity and hydrophilicity of mucins.[34,35] In recent years, a couple of CG models for mucus based on Lennard–Jones (LJ) potentials have been built. It has been used to study mucus aggregation and rheological properties.[36] Shi *et al.* investigated the particle shape effect on the diffusion process within the regular and random mucus networks.[37,38] Yet, a common problem for these LJ models is that they lack physical governing equations for setting interaction parameters, which hinders the transferability of simulating different types of mucins and nanoparticles. Also, these studies overlooked the molecular diversity and heterogeneity of mucus.

In this work, we constructed a CG mucus model at the mesoscale based on the DPD potential, as DPD allows for a more precise description of the hydrophilic/hydrophobic interactions between mucus and nanoparticles. To capture the complexity of the mucus network and mimic the environment of colorectal cancer[18,20], we modeled the two most abundant glycoproteins, Muc2 and Muc5AC, instead of simulating only one type of glycoprotein. We studied the pore size variations of the mucus network under different molecular compositions. Then, we chose one type of widely used drug nanoparticles, PEG, to investigate the diffusion dynamics as PEG is electrostatically neutral and muco-penetrating.[1] Experimental measurements were also conducted to validate the calculations of diffusion coefficients. Our model closely matched our experimental data, offering a cost-effective and efficient method to predict drug and nanoparticle permeability through mucus - a cornerstone in designing drug delivery systems that can penetrate the mucus layer and effectively reach their intended target sites. Furthermore, we utilized machine learning fingerprints proposed by Pinholt[39] to analyze the traces of nanoparticles and conducted a mechanistic study to explain important features for nanoparticle muco-diffusion.

Materials and Methods

Mucus collection. For mucus collection, we modified the method used by Capon *et al.*.[40] In brief, the human colorectal adenoma cell line HT29-MTX-E12, which adopts a goblet-like phenotype, was cultured in 75 cm^2 plastic flasks in Dulbecco's Modified Eagle's Medium (DMEM) supplemented with 10% fetal bovine serum (FBS) for 21 days after confluence. On day 21, the serum-containing medium was replaced

by advanced DMEM/F12 (Gibco) without serum to reduce mucus contamination by foreign proteins. On day 22, the serum-free culture medium was discarded, and the flasks were gently rinsed with Dulbecco's phosphate-buffered saline (DPBS) several times. After that, the cells were incubated for 1 h at 37 °C in DPBS with 0.5 mM forskolin to release the mucus layer. The mucus covering the cells was then gently removed in DPBS (with calcium and magnesium, pH=7.4) and used immediately or stored at -20C. For total mass determination, freshly collected mucus was weight and subsequently lyophilized. The water content was determined by dividing the dry to wet weight.

Mechanical characterization of *in vitro* mucus. A rotational rheometer DHR-3 (TA instruments) was used to investigate the viscoelastic characteristics and apparent viscosity of freshly isolated mucus by applying frequency and flow sweeps. First, the linear viscoelastic region was determined using an amplitude sweep at a constant frequency of 1 rad/s using a 40 mm parallel plate geometry. The mucus' viscoelastic properties in terms of loss (G") and storage (G') moduli were then determined using frequency sweeps performed between 0.01 to 100 rad/s at a 0.5 μNm constant torque with 5 to 10 measurement points per decade and 300 um separation gaps. The mucus' apparent viscosity was measured using flow sweeps in steady mode with a cone and plate geometry (40 mm cone diameter, 63 um truncation). The samples were subjected to shear rates between 0.1 to 100 s^{-1}, with a 300 s equilibration time and 300 um separation gaps. Amplitude, frequency, and flow sweeps were all performed in DPBS with calcium and magnesium (pH=7-7.2) at 25 °C using three different cell culture batches and at least two samples per batch.

Preparation of PEG-coated nanoparticles. Polyethylene glycol (PEG)-coated nanoparticles were prepared using a carbodiimide coupling reaction.[41,42] Briefly, FluoSpheres Carboxylate-Modified Microspheres (ThermoFisher Scientific) with sizes of 100, 200, and 500 nm in diameter at 2% solid concentration were loaded into dialysis tubes (Float-A-Lyzer, 3.5 - 5 kD). The tubes were submerged in 100 mM of monohydrate [2-(N-Morpholino)-ethanesulfonic acid] (MES) buffer, pH 6, for 2 h under constant low stirring. Subsequently, the tubes were transferred to a solution containing 15 mM (1-ethyl-3-(3-dimethylaminopropyl)carbodiimide hydrochloride) (EDC), 5 mM N-Hydroxysulfosuccinimide sodium

salt (NHS), and 50 mg of methoxypolyethylene glycol amine (mPEG-NH2) in MES buffer for 30 min. The bags were then submerged into a solution of 50 mM boric acid and 36 mM sodium tetraborate, pH 8.5, with NHS and mPEG-NH2 at the same concentrations as before. The reaction was left to proceed overnight with constant slow stirring. At the end of the incubation period, the nanoparticles were washed in pure borate buffer, ending with DPBS using a dialysis tube of 20 kDa cut-off (Float-A-Lyzer). Purified PEG-coated nanoparticles were stored at 4C. The hydrodynamic ratio of the PEG-coated nanoparticles was measured in DPBS by dynamic light scattering using a Malvern Nano Zetasizer.

Single particle tracking (SPT). HT29-MTX-E12 cells were cultured on coverslips for 21 days. On day 22, the culture media was replaced for DMEM/F12 media and cells were incubated for one additional day. After that, the coverslips were gently rinsed several times with DPBS without calcium and magnesium and incubated for 10 min with PEG-coated nanoparticles diluted at 1:1000 in DPBS for 100 and 200 nm nanoparticles. For 500 nm nanoparticles, 2:1000 dilution was used from a 2% stock concentration. For tracking single particles within mucus, the coverslips were flipped upside down and imaged using an Elyra Super Resolution Microscope (Zeiss) with a 63X/1.4 oil objective and a sCMOS TV2 camera. Since the mucus layer produced by the HT29-MTX-E12 cells is not continuous, we conducted SPT imaging near the cell monolayer to ensure accurate tracking of the nanoparticles within the mucus layer rather than in the surrounding liquid. Time series containing 500 frames were collected at 0.05 s step time for at least 3 biological replicates and at different locations over the cell monolayer. The same imaging parameters were used for capturing the nanoparticle motion in aqueous solution (DPBS).Single particle trajectories were analyzed using the Trackmate plugin for ImageJ, using the DoG detector and the LAP tracker options. Frame-to-frame linking was limited to 1 um. Recovered particle trajectories and diffusion coefficients were then processed in MATLAB using the msdanalyzer class.[43]

Coarse-grained model of mucins and nanoparticles. We built a coarse-grained (CG) model of mucins in which mucin chains are represented by the bead-spring model. The Muc2 and Muc5AC molecules consist of hydrophobic protein beads (type *h*), which represent the N-terminals, C-terminals and cysteine-rich domains, and hydrophilic beads (type *g*), which represent the glycosylated regions. We estimated the

location and range of the N-terminal, C-terminal, and cysteine-rich domains based on the amino acid sequences of the Muc2 (UniProt: Q02817) and Muc5AC (UniProt: T1S9D5).[44] Thus, the ratio and the position of type *h* beads for each mucin can be adjusted in accordance with their respective amino acid sequences. Type *p* beads packed into spherical shells forming PEG-coated nanoparticles. Figure 1 shows the structures of Muc2, Muc5AC, and the nanoparticles. We also added water beads (type *w*) to simulate the aqueous diffusional environment. The snapshots for nanoparticles with various sizes in mucus were provided in the Supplementary Materials (Figure S1).

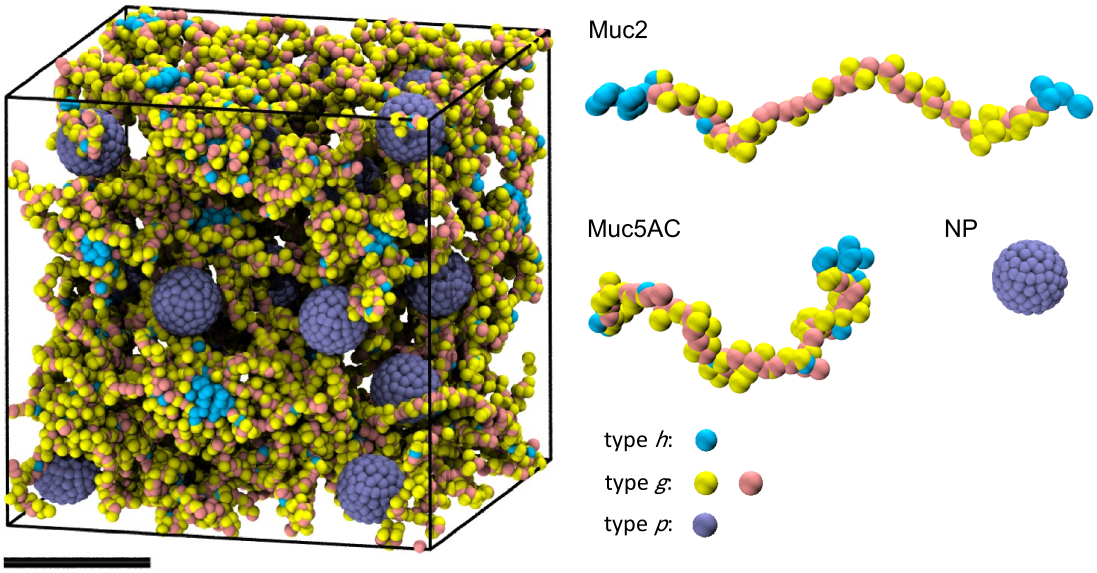

Figure 1. Coarse-grained model (left) of the nanoparticles in the mixture of Muc2 and Muc5AC. The cyan beads represent N-terminal, C-terminal, and cysteine-rich domains. The yellow and pink beads represent the glycosylation regions. Yellow beads denote the side chains linked to the backbones. The iceblue beads represent nanoparticles. Water beads are invisible. The scalebar denotes 10 length units (10 r_0). The structures of each individual component, *i.e.*, Muc2, Muc5AC, and nanoparticles are shown on the right.

The dimensions of the mucin molecules in the simulation were determined according to previous literature.[34,45–48] First, the number of beads in the mucin backbone were polydisperse, which obeyed a Gaussian distribution with a mean of 50 beads and a standard deviation of 3, the value of which were chosen to be approximately proportional to the measurement results.[45] An average of two beads made up each side chain, resulting in the ratio of the diameter to the mucin length comparable with the observation from the microscope and the previous simulation model.[34,46] Additionally, hydrophilic beads accounted

for 87% of the total mucins in our model, which was close to the mass proportion of 80% or 90% mentioned in the literature.[47,48]

Force field of the CG model. To model the interactions between beads, we adopted the interaction potential from the dissipative particles dynamics (DPD) method, as it captures the hydrophilic-hydrophobic relationship in detail between different types of beads.[49] The interaction forces in the DPD model within the cut-off radius r_c are defined as the sum of the conservative force $F_{ij}{}^{C}$, dissipative force $F_{ij}{}^{D}$, and random force $F_{ij}{}^{R}$. The complete form of potential equations can be referred to Groot's work.[49] As DPD uses normalized non-dimensional units, the cut-off radius r_c was set to one unit length ($r_c = r_0$) and the temperature was 1 k_bT. The radius of one bead is $0.52r_0$, which is determined by coarse-graining 16 water molecules in one bead and the bead density of $\rho {r_c}^3 = 3$. The values of the maximum repulsive parameters a_{ij} used in our model are listed in Table 1. The parameter between PEG and water a_{pw} was adopted from Luo *et al*.[50], and other parameters a_{ij} were adopted from Moreno *et al*.[34] The repulsive parameters between PEG and hydrophobic protein beads a_{ph} and between PEG and glycan beads a_{pg} were calculated from Hansen solubility parameters[51]:

$$a_{ij} = a_{ii} + 3.27 \times \frac{V_b}{k_bT}\left(\left(\delta_{d,i} - \delta_{d,j}\right)^2 + 0.25\left(\delta_{p,i} - \delta_{p,j}\right)^2 + 0.25\left(\delta_{h,i} - \delta_{h,j}\right)^2\right),$$

which were finally chosen to be 40 k_bT/r_0 and 55 k_bT/r_0, respectively. The detailed reasoning and validation is provided in the Supplementary Material Section II. The parameter for the dissipative force γ was set to 4.5. In addition, we also defined the bond and the angle potentials as follows. The adjacent beads in a backbone or in a side chain were connected by harmonic bonds: $U_b = K_b\left(r_{ij} - r_{0,b}\right)^2$, where the stiffness K_b was set to 25 k_bT, and the equilibrium distance $r_{0,b}$ was set to 0.7 r_0.[34] Considering the straight morphology of the tandem repeat regions in the main peptide chains[52], the adjacent three *g* beads in the backbone were connected by a harmonic angle: $U_a = K_a\left(\theta_{ijk} - \theta_{0,a}\right)^2$, where the equilibrated angle $\theta_{0,a}$ was 180 degrees and the stiffness was set to 2.5 k_bT.

Table 1. The maximum repulsive parameters a_{ij} used in the DPD model.

Maximum repulsive parameters $a_{ij}(\mathbf{unit}: k_bT/r_c)$				
	h	g	p	w
h	25			
g	60	25		
p	40	55	25	
w	60	25	26.05	25

Simulation Protocol. We first randomly generated polydisperse mucin molecules in the simulation box and equilibrated them by running 600,000 steps of NVE ensemble followed by 10,000,000 steps of NVT ensemble (dt = 0.01). Then, if necessary, we created intermolecular disulfide bonds if the distance between any two *h* beads was smaller than $2r_0$. After adding disulfide bonds, we ran 10,000,000 steps of NVT ensemble to re-equilibrate the system. Nanoparticles were randomly added in the empty spaces within the mucin network after the crosslinked mucins were equilibrated. The radii of nanoparticles were $0.5r_0$, $1.0r_0$, $1.5r_0$, $2.0r_0$, $3.0r_0$, and hence their volumes varied as well. We added nanoparticles into the model systems such that the volume of nanoparticles was 0.2 times of the volume of the mucins. The diffusions were conducted under the NVT ensembles for at least 1,000,000 steps (dt = 0.02) to ensure that the nanoparticles were in the normal diffusion mode. During the diffusion, each nanoparticle was treated as a rigid body, so every *p* beads in a same nanoparticle had the same velocity.

Machine-learning Analysis of Nanoparticle Diffusion. We employed a recently-developed machine-learning framework[39] to quantify the fingerprints of nanoparticle diffusion and to classify the different sizes of nanoparticles. In the previous paper, the authors defined 17 fingerprints as the features for training purposes. Here, we adopted 4 features, MeanMSD, Trappedness, Fractal dimension, Efficiency, and developed 3 new features, T1, T2, and T3, which were explained in the Results section. We fed these features into logistic regression model using scikit-learn's function LogisticRegression(). Due to the existence of more than two types of nanoparticles, we performed multinomial logistic regression. For the sake of generalizability, we randomly spilt 60% of the data into the training set and 40% of dataset into the test set and obtained the average accuracy from 200 trials.

Results

Rheology Measurement and Pore Size Characterization:

To investigate the mechanical and barrier properties of human intestinal mucus, we collected intact mucus from the *in vitro* culture of human goblet cells (HT29-MTX-E12). Compared to other cell lines, HT29-MTX-E12 cells develop a confluent monolayer of mature goblet cells and produce a mucus layer with a thickness comparable to what is observed in humans *in vivo*.[53] We assessed the viscoelastic properties of this mucus within the linear viscoelastic range through dynamic oscillatory rheology. We quantified the material response to deformation in terms of the storage modulus (G') and loss modulus (G") by performing frequency sweeps under a constant deformation force. G' reflects the material's resistance to deformation and its ability to store energy. In contrast, G" characterizes the material's liquid-like behavior, indicating its capacity to dissipate energy as heat. G" also provides information about the material's ability to flow or deform without resistance.[53–55]

Frequency sweep experiments revealed that both G' and G" were frequency independent, indicating that the mucus is a cross-linked gel (Figure 2). The mucus displayed a finite G' value over a significant range of frequencies, a characteristic commonly associated with a solid-like viscoelastic response.[54] At 1 rad/s, the values for G' and G" modulus varied between 0.41-34 Pa and 0.04-4.4 Pa, respectively, which are comparable to those reported for human gastric mucus at a similar frequency range (G'=13-21 Pa and G"=1.8-3.2 Pa).[56] G' was also more than seven times larger than the values for G" for all the samples, further demonstrating the solid-like behavior of the mucus. In practical terms, a high G' indicates that the material is relatively rigid and can withstand deformation with minimal energy loss. Conversely, a low G' suggests a more fluid-like and easily deformable material. Similarly, a high G" implies greater viscosity and energy dissipation, while a low G" indicates higher elasticity and minimal energy dissipation.[54] This viscoelastic behavior is typical in other soft tissues and biological materials.[57] Rheological analysis has shown that soft tissues exhibit a G" around 10% to 20% of their G' moduli at 1Hz.[58]

Mesh size is an important structural feature of polymer networks and affects the diffusion of particulate material within mucus.[55,59,60] Thus, beyond characterizing the viscoelastic behavior, we also estimated the mucus' average mesh size from the frequency sweep experiments[55] based on the elastic blob theory[61,62], $\xi = \left(\frac{G'}{k_B T}\right)^{-1/3}$, where ξ is the pore size and G' is the storage modulus at zero frequency. The average zero-frequency storage modulus was 0.42±0.025 Pa, yielding an estimated mesh size of 214.04±4.29 nm.

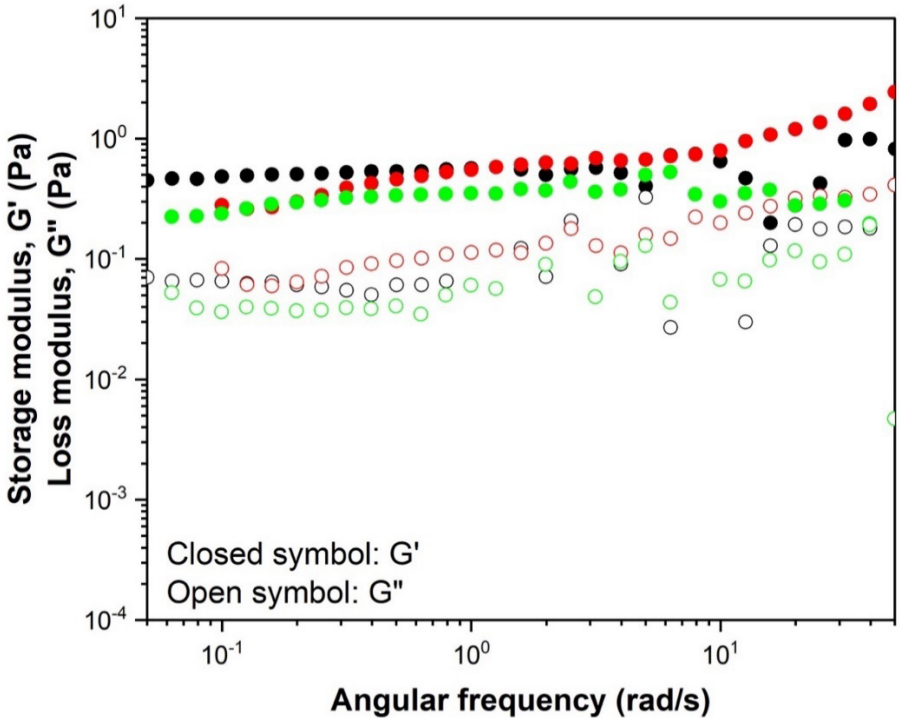

Figure 2. The storage (G', closed circles) and loss moduli (G", open circles) for 3 mucus samples collected from HT29-MTX-E12 cells. Different mucus samples are distinguished by different colors. The frequency-independent G" and G' indicates mucus is a cross-linked gel with solid-like viscoelastic response.

In our computational simulations, we calculated the mesh sizes of mucin under three different weight percentages, namely 5 wt%, 10 wt% and 20 wt%. The mesh sizes are determined by PSDsolv.[63] Since HT29-MTX-E12 cells naturally produce mucus composed of 60% Muc5AC and 40% Muc2,[18,19] we used this ratio in the simulation and tested pure Muc5AC and pure Muc2 as a benchmark (Figure 3). We found that the average mesh sizes were roughly inversely proportional to the mucin weight percentage. For example, the mean pore sizes were $7.76r_0$, $4.69r_0$, and $2.36r_0$ (Muc5AC/(Muc5AC+Muc2) = 0.6) when the weight percentages were 5 wt%, 10 wt%, and 20 wt%, respectively. In addition, the mesh size decreased

as the concentration of Muc5AC increased which was clearly observed in the 5 wt% simulation (p-value < 0.05 between any two groups, and calculations are described in Supplementary Materials Section III). Muc5AC gave rise to a more evenly distributed network structure with smaller mesh sizes due to the presence of more crosslink-able cysteine-rich domains. However, high concentrations of Muc5AC, *e.g.*, 10 and 20 wt%, did not reduce the average mesh sizes to the same extent as in models with 5 wt%. In this case, Muc2 provided sufficient crosslinks distributed throughout the network as hydrophobic N- and C-terminals (explained in greater detail in Supplementary Material Section IV). To choose an appropriate weight percentage for subsequent models, we determined the water content in the mucus collected from the HT29-MTX-E12 cells. As the dry weight accounted for 20% of the wet weight, we used the mucus model of 20 wt% to investigate the dynamics of nanoparticle diffusion (Supplementary Material Section V).

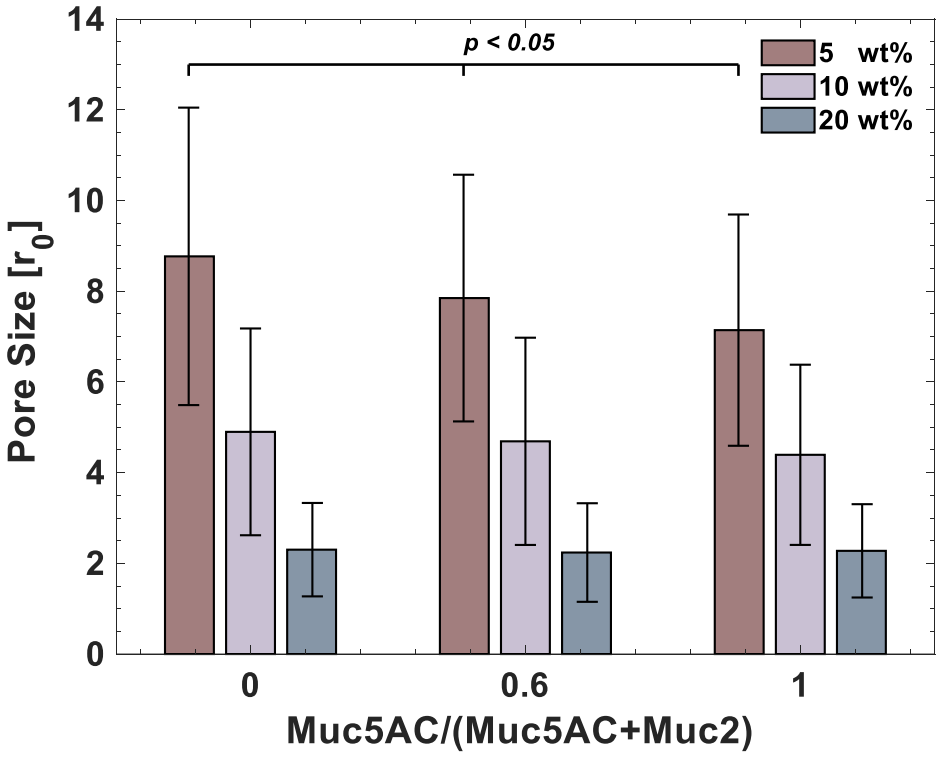

Figure 3. The pore sizes calculated in the simulations for different Muc5AC/(Muc5AC +Muc2) weight ratios and different weight percentages of total mucins, {0, 0.6, 1}×{5 wt%, 10 wt%, 20 wt%}. *P*-value is calculated by the two-samples t-test. For cases where the weight percentage is 5 wt%, the *p*-value is smaller than 0.05 between any two groups.

Nanoparticle Diffusion

We employed single-particle tracking to measure the movements of PEG-coated nanoparticles within mucus, measuring 100, 200, and 500 nm in diameter. As revealed by Figure 4 (a)-(f), all nanoparticle (NP) sizes had diminished ranges of motion within the mucus compared to the aqueous environment (DPBS). However, particles nearing the mucus' mesh size encountered a significant restriction in their range of motion. This reduction was particularly pronounced for nanoparticles that are 500 nm in diameter, where their explored area decreased twofold compared to their mobility in DPBS. The diffusion coefficient quantifies the dynamics of nanoparticles and can be obtained, according to the Einstein relation, from the slope of the mean squared displacement (MSD) with respect to time (Figure 4 (g)-(i)).[64] The diffusion coefficients were calculated by fitting the linear equation, $MSD = 4Dt$, the values of which were further used in validating the simulation model.

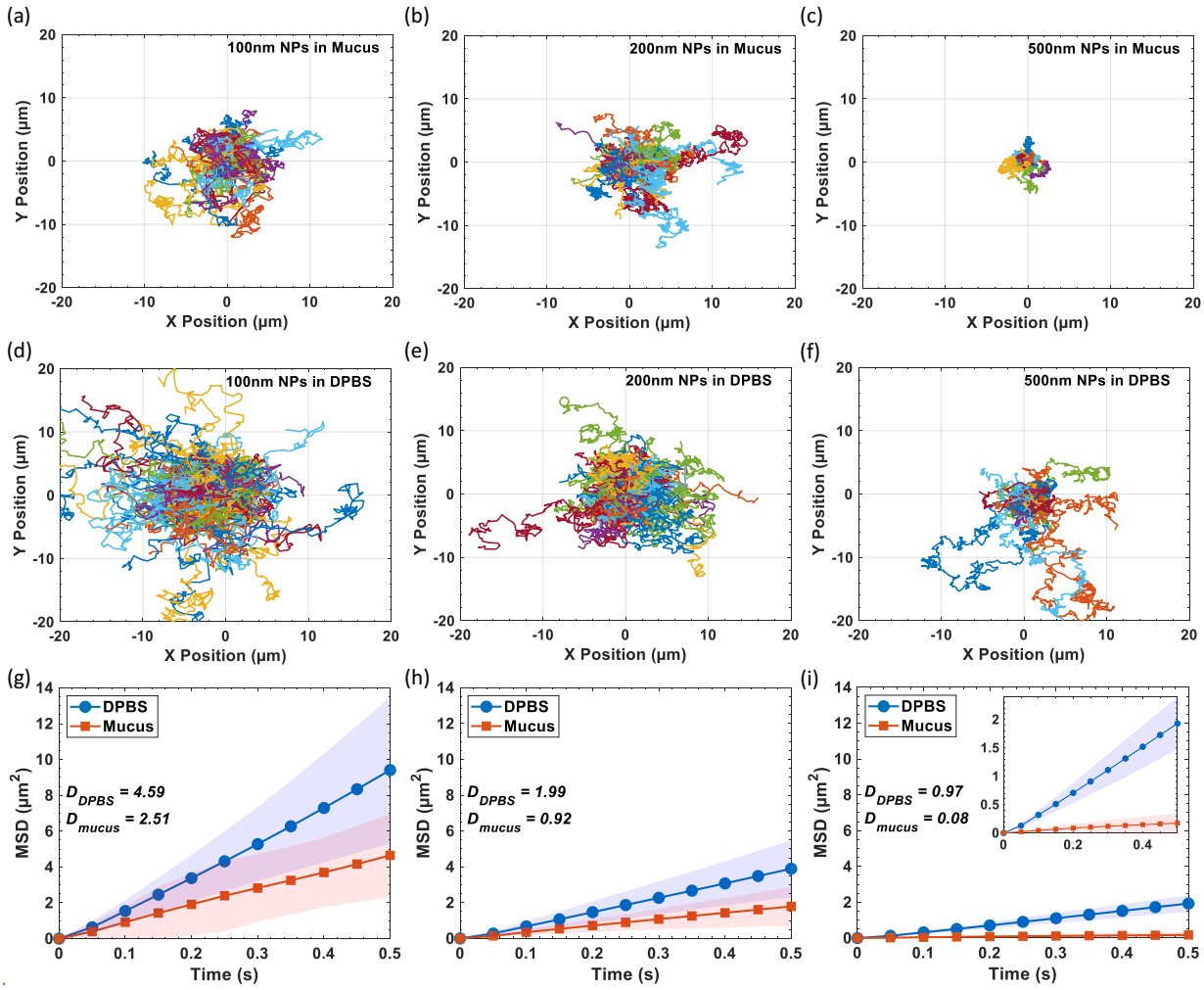

Figure 4. (a)-(c) The 2D trajectories in x-y plane of 100 nm, 200 nm, 500 nm nanoparticles diffused in mucus. (d)-(f) The 2D trajectories in x-y plane of 100 nm, 200 nm, 500 nm nanoparticles diffused in DPBS. Each colored line represents the trajectory of one particle. All trajectories were superimposed at the origin. (g)-(i) The MSD curves for 100 nm, 200 nm, and 500 nm nanoparticles, respectively. The blue and red curves represent the MSDs in DPBS and Mucus. The shaded area denotes the standard deviation of the MSD. The diffusion coefficients *D* were obtained by the linear fitting of the mean MSD, which were shown in the figures.

The van Hove correlation function provides crucial insights into the spatiotemporal behavior of particles undergoing diffusion or motion within a complex environment.[59,65] It is a mathematical construct that describes the probability of finding a particle at a distance Δx from a reference particle at a given time Δt:

$$\Delta x = x(t + \Delta t) - x(t).$$

Figure 5 shows the van Hove correlation functions for 100 nm, 200 nm, and 500 nm nanoparticles in mucus networks when Δt equal to 0.05s, 0.1s, and 0.15s. For nanoparticles of any size, the van Hove correlation function exhibited a statistical Gaussian-like distribution, except for disturbance when Δx is close to zero. Among various nanoparticle sizes, the smallest nanoparticles were able to diffuse the most freely within the mucus. For both 100 nm and 200 nm particles, as Δt increased, the van Hove distribution decreased and broadened, implying increased diffusion over time. Conversely, the 500 nm particles' distributions remained relatively unchanged, suggesting effective entrapment within the mucus network.

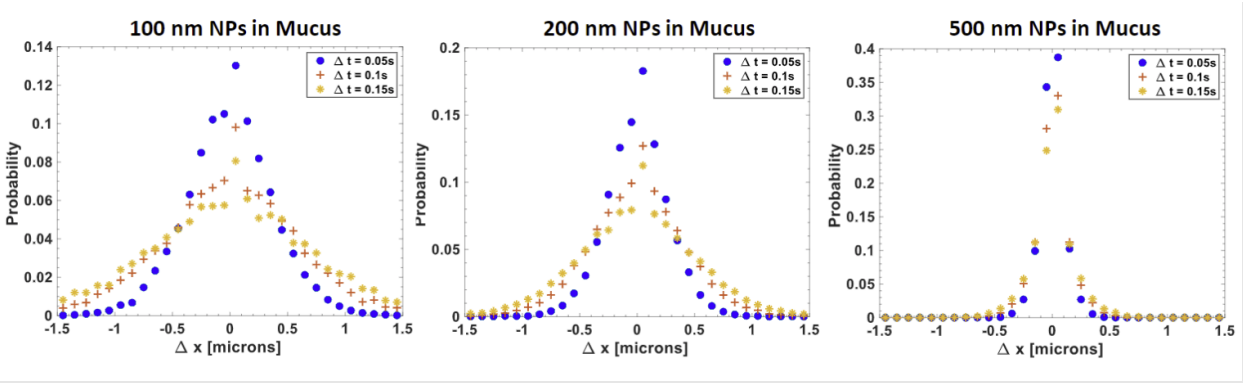

Figure 5. The van Hove correlation functions of 100 nm, 200 nm, and 500 nm nanoparticles diffusing in mucus at the time durations Δt of 0.05s, 0.1s, and 0.15s. The narrow peaks of 500 nm nanoparticles revealed that they were effectively trapped within the mucus.

In terms of the computational model, we simulated the diffusion of nanoparticles with different sizes. The range of nanoparticle sizes were chosen based on the time-averaged mesh size distribution of mucins (Figure 6 (a)), which was normally distributed with a mean of $2.16r_0$ in radius. Compared with the experimental mesh size of 214.04±4.29 nm in diameter, the scaling ratio of our model is around 1:50, *i.e.*, $r_0 \approx 50$ nm. We created nanoparticles with radii of $0.5r_0$, $1.0r_0$, $1.5r_0$, $2.0r_0$ and $3.0r_0$ into our models, covering the range where the nanoparticles are smaller and larger than the average mesh size. Importantly, the chosen nanoparticle sizes fall into the diameters (10 nm to 400 nm) commonly used in nanoparticle-based therapeutics.[66–68]

We then examined the MSD curves and the diffusion coefficients of the nanoparticles in the model. However, due to the relatively small time scale in the simulation, we observed three distinct regimes during nanoparticle diffusion: (1) the ballistic regime where the MSD is proportional to t^2; (2) the subdiffusive regime where the MSD is proportional to t^β ($\beta < 1$); and (3) the normal diffusion regime (Fickian diffusion) where the MSD is proportional to t.[69] The diffusion coefficient describes the diffusion rate of nanoparticles within the normal diffusion regime. To distinguish the three regimes, we analyzed the trend of MSD/time versus time (Figure 6 (b)). Initially, the nanoparticles were in the ballistic regime where the curve sloped upwards with time. Large nanoparticles ($r = 3.0r_0$) underwent longer periods of ballistic diffusion than small nanoparticles ($r = 0.5r_0$). Subsequently, the curves began to slope downwards, indicating that the nanoparticles transitioned into the subdiffusive regime. Eventually, all the curves plateaued when the nanoparticles attained the normal diffusion regime, where the diffusion coefficient was computed.

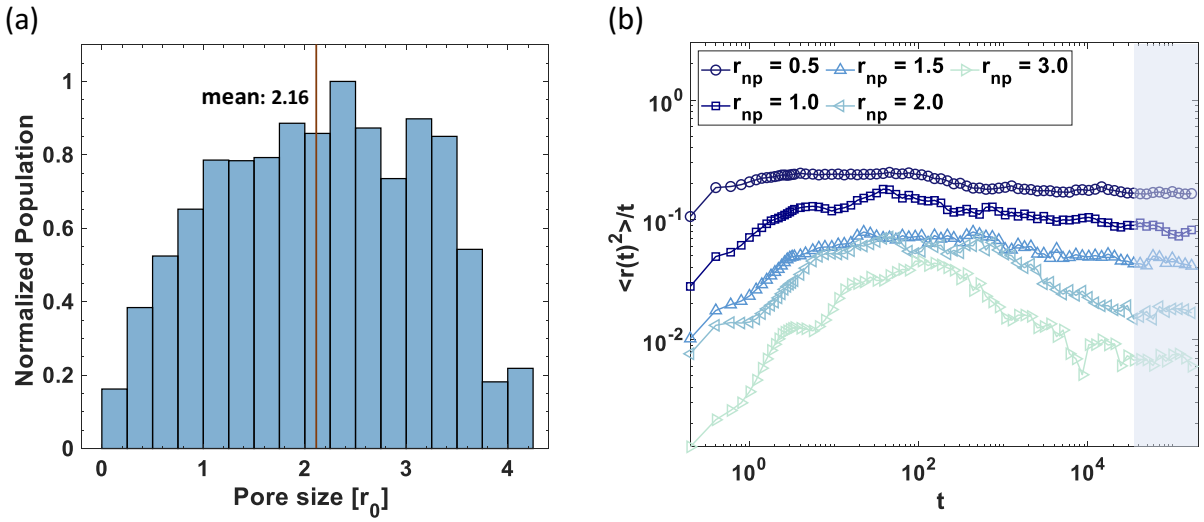

Figure 6. (a) The time-averaged pore size distribution of mucus after equilibrium where the mean pore size, denoted by the vertical red line, is $2.16r_0$. (b) The log-log plot of the mean squared displacements divided by time for nanoparticles radii of $0.5r_0$, $1.0r_0$, $1.5r_0$, $2.0r_0$, and $3.0r_0$. The shaded area denotes the normal diffusion states, and the diffusion coefficients were calculated using this region.

To comparatively analyze the simulation and experimental results, we normalized both diffusion coefficient and the nanoparticle size. The diffusion coefficient in mucus D_m was normalized by dividing the diffusion coefficient of the same nanoparticle in DPBS buffer D_w (pure water in simulation). The ratio D_m/D_w can help to unveil the influence of mucus network on the diffusion process of nanoparticles. As we used the spherical and non-charged PEG-coated nanoparticles in the experiment, the measured diffusion coefficients in DPBS were theoretically calculated by Stokes-Einstein equation[70]:

$$D_w = \frac{k_B T}{3\pi\eta d},$$

where η is the viscosity of the diffusion media (0.001 Pa·s) and d is the diameter of nanoparticles. In our simulations, D_w was obtained by putting the same nanoparticles in pure water beads. To unify the size scale of simulation and experiment, we defined the confinement ratio r_{eff}/ξ as the effective size of nanoparticles to the mucus mesh size. In experiments, the effective size r_{eff} was the actual hydrodynamic diameter of nanoparticles measured by dynamic lighting scattering. For the nanoparticles with nominal diameter of 100 nm, 200 nm, and 500 nm, we measured their hydrodynamic diameter as 110.30±0.79 nm, 216.70±2.48 nm, and 495.53±7.71 nm. In simulation, the effective size r_{eff} was defined as the radius of the nanoparticle plus the radius of the bead, which is $0.52r_0$ as defined in the Method section. The pore size ξ in the experiment and in simulation were 214.04 nm and $2.16r_0$, respectively. Figure 7 presents dimensionless diffusion coefficients and sizes, depicting the alignment between the model and measurements. The diffusion coefficient decreased from 0.6 to 0.1 when the confinement ratio varied from 0.5 to more than 2. This trend, shown in Figure 7, parallels the van Hove distribution in Figure 5, indicating hindered diffusion for a confinement ratio ≤ 1 and effective restriction for larger nanoparticles (confinement ratio > 2). Furthermore, we employed the hopping model, proposed by Cai and Rubinstein[71], to quantify the connection between the nanoparticle size d and the diffusion coefficient in mucus network D_m:

$$D_m = \frac{{\xi_c}^2}{\tau_0 N^2 \phi}\left(\frac{bN^{0.5}}{d}\right)e^{-d^2/Nb^2}.$$

We fixed the number of monomer units in between cross-links as the average beads per mucin chain (N = 50). The polymer fraction ϕ was 20%, which was determined by the dry mass and wet mass of mucus samples. As the mucin chains can be treated as worm-like chains, the Kuhn length b of which can be approximated by their persistence length (b = 44 nm).[45,72] Then, we adjusted the coefficient ${\xi_c}^2/\tau_0$ to be 4.35×10^{-10} cm^2/s (ξ_c is the correlation length of mucus and τ_0 is the monomer relaxation time) to fit our data points. The value of the coefficient ${\xi_c}^2/\tau_0$ in our mucus model is one order of magnitude lower than the coefficient where nanoparticles diffused in a non-biological polymer gel (${\xi_c}^2/\tau_0=2.9\times10^{-9}$ cm^2/s).[62] This suggests that the mucus possesses a denser, intricate network with extended relaxation times, consequently resulting in slower dynamics.

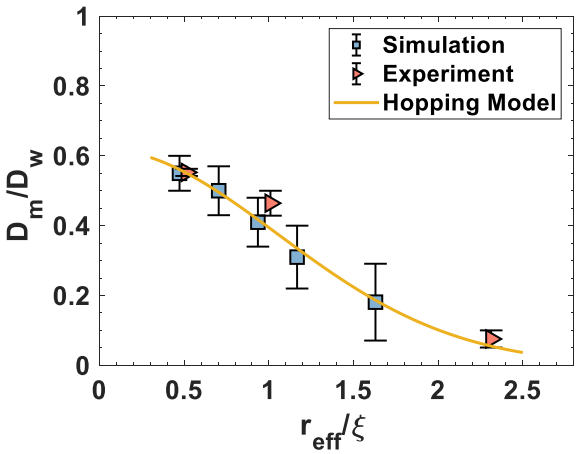

Figure 7. The dependence of the normalized diffusion coefficient (D_m/D_w) to the normalized size (r_{eff}/ξ). The yellow line was the hopping model used to fit the simulation and experimental data points (mean squared error is 1.20e-3).

Machine-learning Classification and Diffusional Feature Analysis

By addressing the complex and diverse diffusion patterns inherent in biological systems, other authors recently established a machine-learning paradigm that contains 17 descriptive features obtained from the trajectories of single nanoparticles.[39] The paradigm not only enables accurate particle classification but

also unveils crucial mechanistic insights by identifying key differences among diffusional features. Therefore, we adopted and modified their ML framework to classify and analyze single-nanoparticle trajectories from our simulation.

The features we used are listed in

Table 2. We picked some representative features, including MeanMSD, fractal dimension, trappedness, and efficiency. The MeanMSD is the average MSD counted to half of the trajectories. The fractal dimension is defined as

$$D_f = \frac{\ln(N)}{\ln(N) + \ln(\frac{d}{L})},$$

where N, d, and L are the number of steps in the trajectory, the maximum distance between two points in the trajectory, and total traveling distance, respectively. The trappedness is defined as:

$$\text{Trappedness} = 1 - \exp\left[0.2045 - 0.25117\left(\frac{Dt}{R}\right)\right],$$

which represents the likelihood of a particle characterized by the diffusion coefficient D to exit a circular region with a radius R for during a time interval of t. The efficiency is defined as the logarithm of the ratio of end-to-end length to the total traveling distance:

$$\gamma = \ln\left(\sqrt{\frac{(x_N - x_1)^2 + (y_N - y_1)^2}{(N-1)\left[\sum_{i=2}^{i=N}(x_i - x_{i-1})^2 + (y_i - y_{i-1})^2\right]}}\right).$$

Furthermore, drawing inspiration from the implementation of the Hidden Markov Model for partitioning particle trajectories into distinct diffusion states, we divided trajectories into multiple shorter ones. We then employed the fractal dimension as a criterion to categorize these short trajectories into three diffusion states: ballistic diffusion, normal diffusion, and subdiffusion, denoted by the features T1, T2,

and T3. These features represent the proportions of short trajectories corresponding to each respective diffusion state.

Table 2: List of features used in ML classification.

Feature Name	Description
Fractal Dimension (D_f)	Space-filling-ness of the trajectory
Trappedness	Estimator to determine whether nanoparticle is trapped
Efficiency	The ratio of end-to-end distance to the sum of distance
MeanMSD	The average MSD calculated up to half the trajectory length
T1	The fraction of piece-wise trajectories when $D_f < 1.6$ (ballistic)
T2	The fraction of piece-wise trajectories when $1.6 \leq D_f \leq 2.0$ (normal)
T3	The fraction of piece-wise trajectories when $D_f > 2.0$ (subdiffusive)

Utilizing these features, we employed multinomial logistic regression to classify the sizes of nanoparticles diffusing within mucus. As demonstrated in Figure 8, the ML model achieved an accuracy exceeding 90% for each particle type, even when only a subset of the 17 features suggested in prior studies[39] were utilized. The clustered arrangement of the confusion matrix along the diagonal indicated that the logistic regression model occasionally misclassified a small portion of particles as being of similar size, and there were no large deviations occurring.

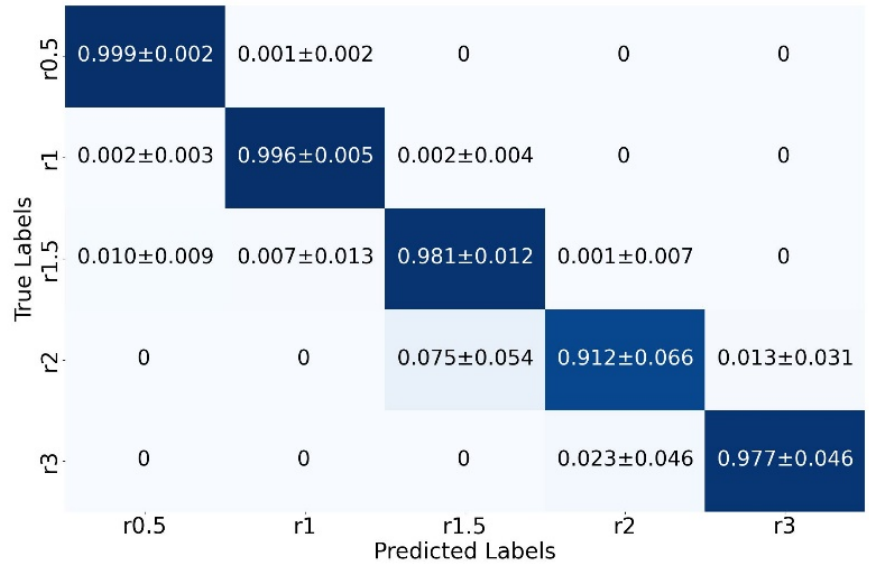

Figure 8. **The confusion matrix of logistic regression model to classify the sizes of nanoparticles. The labels r0.5, r1, r1.5, r2, r3 denote the nanoparticles with radii of $0.5r_0$, $1r_0$, $1.5r_0$, $2r_0$, and $3r_0$, respectively. The numerical mean accuracy (max = 1) and standard deviations were shown in the confusion matrix.**

Subsequently, we analyzed the average values of each feature across different nanoparticles. In Figure 9 (a), it is evident that the MeanMSD exhibited a noticeable reduction as nanoparticle size increased. To quantify this trend, we employed an exponential function, $y = e^{-1.34x+8.83}$, having a low mean absolute percentage error (MAPE) of 3.3%. This observation implies an exponential correlation between MeanMSD and the nanoparticle size. Figure 9 (b) and (c) indicated that increased particle size correlated with reduced efficiency and heightened trappedness. These findings collectively supported the notion that larger particles encountered greater difficulty in traveling extended distances and were more prone to entrapment within the mucus. While the changes in efficiency and trappedness were less pronounced than the MeanMSD disparities, we quantitively examined the significant differences between the smallest particles and the other particles. The calculated *p*-values demonstrated that a significant difference exists between the smallest particles and any particles with r≥2.0. Figure 9 (d) displayed the average and standard deviation of fractal dimensions (D_f) for particles of varying sizes. According to the definition of D_f, a small and nearly 1 corresponds to almost ballistic diffusion. Theoretically, normal diffusion possesses a D_f around 2, while subdiffusion has a D_f exceeding 2. However, our outcomes revealed D_f values slightly below 2 for all particles, a phenomenon also observed by Pinholt.[39] This deviation might

arise from the trajectories' insufficient length. It could be caused by the fact that the trajectories were not long enough. Having the same length of trajectories for all particles, we found that smaller particles had smaller D_f, indicating a propensity towards ballistic diffusion.

Then, we divided the complete trajectory (comprising 8000 frames) of a single particle into 800 shorter trajectories using a window size w of 10. Based on the statistics in Figure 9 (d), we classified ballistic diffusion (T1) when $D_f < 1.6$, normal diffusion (T2) when $1.6 \leq D_f \leq 2.0$, and subdiffusion (T3) when $D_f > 2.0$. Most short trajectories had $D_f < 1.6$, as depicted in Figure 10 (a), indicating their categorization as ballistic diffusion (T1). Interestingly, for the short trajectories, the fraction of ballistic diffusion increased as the increase in the particle size. This trend was opposite to the observation in Figure 9 (d). Because the value of D_f depends on $\ln(d/L)$, we computed the mean $\ln(d/L)$ for all particles across a range of window sizes from 10 to 2500 (Figure 10 (b)) to avoid the artificial error caused by the window size. When w was smaller than 1000, larger particles exhibited higher $\ln(d/L)$, leading to smaller D_f values. The trend reversed when w exceeded 1000, with larger particles demonstrating smaller $\ln(d/L)$, resulting in larger D_f. This result not only verified the correctness of Figure 10 (a), but also unveiled an intriguing diffusion mechanism: over a sufficiently long period, larger particles tend to get trapped and display subdiffusive behavior. However, on a very short time scale, they showcase more ballistic diffusion compared to smaller particles.

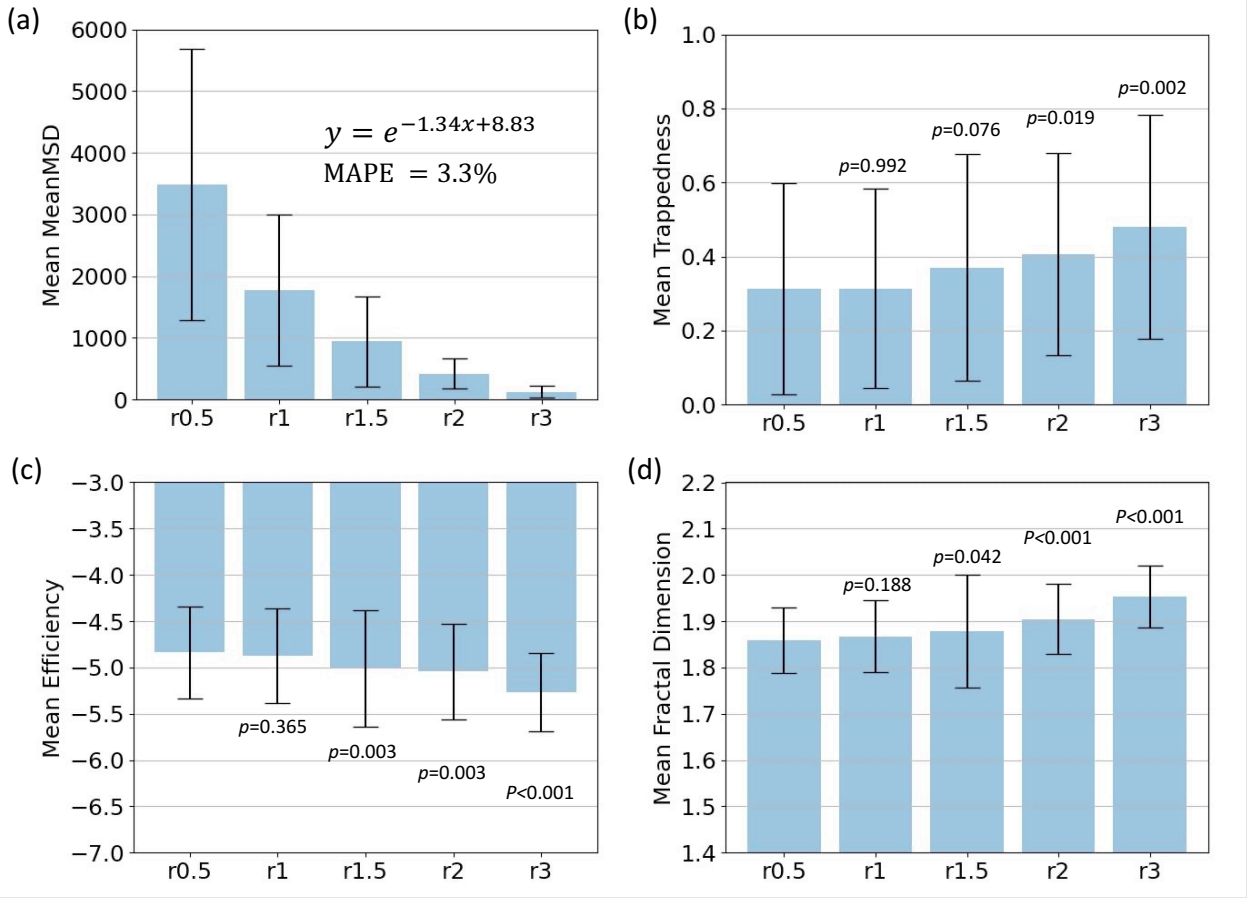

Figure 9. (a) The histograms of the average MeanMSD of nanoparticles with radii of 0.5, 1, 1.5, 2, and 3. The variety of MeanMSD versus radius was fitted by an exponential relation (mean absolute percentage error = 3.3%). The error bars denote the standard deviations. (b) – (d) The average fractal dimension, efficiency, and trappedness of nanoparticles. The *p*-values represent the significant difference between the group and the first group (r = 0.5). There is a significant difference if $p < 0.05$.

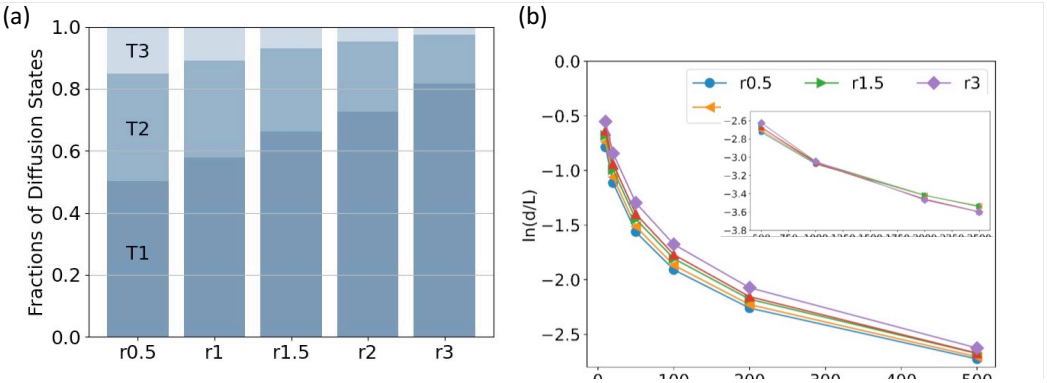

Figure 10. (a) The fractions of three diffusion states derived from short trajectories (w=10). The state T1 (dark blue) represents the ballistic diffusion where $D_f < 1.6$. The state T2 (middle blue) represents the normal diffusion where $1.6 \leq D_f \leq 2.0$. The state T3 (light blue) represents the subdiffusion where $D_f > 2.0$. (b) The variation of the logarithm of end-to-end distance divided by the total traveled distance, ln(d/L), with respect to the window size w. The inset figure shows the variation for window size w ranging from 500 to 2500.

Conclusions

In this study, we developed a coarse-grained particle-based model for the human gastrointestinal mucus and diffusive PEG-coated nanoparticles. To validate the model, experimental measurements were performed to characterize the mucus and diffusion processes of nanoparticles. Frequency sweep experiments revealed covalent cross-linking in the mucus, giving it solid-like behavior, with an average mesh size of 214 nm. Analyzing single particle traces and van Hove correlation functions for nanoparticles of 100 nm, 200 nm, and 500 nm in diameter, we found that 500 nm nanoparticles, the ones larger than the pore size, were trapped effectively in the mucus polymeric network. From computational simulations, our model captured important mucus molecular structures (Muc2 and Muc5AC), allowing us to study pore size dependence on chemical composition and mucus concentration. Given the significance of pore size for the permeability of nanoparticles, it underscores the necessity of simulating various mucin components. To match the experimental conditions, we simulated nanoparticle diffusion in 20 wt% mucus composed of 60% Muc5AC and 40% Muc2. Upon normalizing the diffusion coefficient and nanoparticle sizes, we observed agreement between the simulated and experimental diffusion coefficients. A mathematical model, namely the hopping model, closely matched both simulation and experimental outcomes. In addition, we employed 7 diffusional fingerprints for particles, based on which we trained a logistic regression model to differentiate particle sizes. By carefully examining the fingerprints, we further discovered that larger nanoparticles tend to be trapped in mucus over longer durations, while they exhibit more ballistic diffusion over shorter time spans. Based on the studies discussed above, our model effectively characterized the diffusion of the surface-neutral muco-penetrating PEG-coated nanoparticles in the human colorectal adenoma environment. Yet, CG models under physiological conditions and disease states need to be further validated due to the changes in mucus compositions. By tuning the abundance of disulfide bonds and intramolecular bonds in the model, mucus aggregation and particle diffusion processes can also be examined under the condition of mucolytic enzyme degradation, which is another strategy to enhance the penetration ability of particulate materials.[1,73] In terms of the modeling of nanoparticles, the current model can be extended to study irregularly shaped or charged nanoparticles.

The Slater smearing charge distribution method can be used to augment our model for such investigations.[74,75] Overall, our models will serve as a foundation for understanding and predicting mucus-nanoparticle interactions, thereby providing a promising platform for future work on the diffusion of nanoparticle-based therapeutics in the human gastrointestinal mucus.

Acknowledgments

J.Y. acknowledges support from the US National Science Foundation under awards EFMA-2223785, as well as the computational resources provided by the NSF Advanced Cyberinfrastructure Coordination Ecosystem: Services & Support program under award TG-BIO210063.

References:

1. Xu, C., Xu, H., Zhu, Z., Shi, X. & Xiao, B. Recent advances in mucus-penetrating nanomedicines for oral treatment of colonic diseases. *Expert Opin. Drug Deliv.* **20**, 1371–1385 (2023).

2. Watchorn, J. *et al.* Untangling Mucosal Drug Delivery: Engineering, Designing, and Testing Nanoparticles to Overcome the Mucus Barrier. *ACS Biomater. Sci. Eng.* **8**, 1396–1426 (2022).

3. Chen, D., Liu, J., Wu, J. & Suk, J. S. Enhancing nanoparticle penetration through airway mucus to improve drug delivery efficacy in the lung. *Expert Opin. Drug Deliv.* **18**, 595–606 (2021).

4. Subramanian, D. A., Langer, R. & Traverso, G. Mucus interaction to improve gastrointestinal retention and pharmacokinetics of orally administered nano-drug delivery systems. *J. Nanobiotechnology* **20**, 362 (2022).

5. McShane, A. *et al.* Mucus. *Curr. Biol.* **31**, R938–R945 (2021).

6. Gustafsson, J. K. & Johansson, M. E. V. The role of goblet cells and mucus in intestinal homeostasis. *Nat. Rev. Gastroenterol. Hepatol.* **19**, 785–803 (2022).

7. Liu, C., Jiang, X., Gan, Y. & Yu, M. Engineering nanoparticles to overcome the mucus barrier for drug delivery: Design, evaluation and state-of-the-art. *Med. Drug Discov.* **12**, 100110 (2021).

8. Gao, X. *et al.* Mucus adhesion vs. mucus penetration? Screening nanomaterials for nasal inhalation by MD simulation. *J. Controlled Release* **353**, 366–379 (2023).

9. Neves, J. das, Arzi, R. S. & Sosnik, A. Molecular and cellular cues governing nanomaterial–mucosae interactions: from nanomedicine to nanotoxicology. *Chem. Soc. Rev.* **49**, 5058–5100 (2020).

10. Sosnik, A. & Menaker Raskin, M. Polymeric micelles in mucosal drug delivery: Challenges towards clinical translation. *Biotechnol. Adv.* **33**, 1380–1392 (2015).

11. Zierden, H. C. *et al.* Avoiding a Sticky Situation: Bypassing the Mucus Barrier for Improved Local Drug Delivery. *Trends Mol. Med.* **27**, 436–450 (2021).

12. Allen, A. The Structure and Function of Gastrointestinal Mucus. in *Attachment Of Organisms To The Gut Mucosa* (CRC Press, 1984).

13. Lutz, T. M., Kimna, C. & Lieleg, O. A pH-stable, mucin based nanoparticle system for the co-delivery of hydrophobic and hydrophilic drugs. *Int. J. Biol. Macromol.* **215**, 102–112 (2022).

14. Song, C. *et al.* Intestinal mucus components and secretion mechanisms: what we do and do not know. *Exp. Mol. Med.* **55**, 681–691 (2023).

15. Liu, Y. *et al.* Orchestration of MUC2 — The key regulatory target of gut barrier and homeostasis: A review. *Int. J. Biol. Macromol.* **236**, 123862 (2023).

16. Fass, D. & Thornton, D. J. Mucin networks: Dynamic structural assemblies controlling mucus function. *Curr. Opin. Struct. Biol.* **79**, 102524 (2023).

17. Hansson, G. C. Mucins and the Microbiome. *Annu. Rev. Biochem.* **89**, 769–793 (2020).

18. Elzinga, J., van der Lugt, B., Belzer, C. & Steegenga, W. T. Characterization of increased mucus production of HT29-MTX-E12 cells grown under Semi-Wet interface with Mechanical Stimulation. *Plos One* **16**, e0261191 (2021).

19. Navabi, N., McGuckin, M. A. & Lindén, S. K. Gastrointestinal cell lines form polarized epithelia with an adherent mucus layer when cultured in semi-wet interfaces with mechanical stimulation. *PloS One* **8**, e68761 (2013).

20. Walsh, M. D. *et al.* Expression of MUC2, MUC5AC, MUC5B, and MUC6 mucins in colorectal cancers and their association with the CpG island methylator phenotype. *Mod. Pathol.* **26**, 1642–1656 (2013).

21. Rico, S. D. *et al.* MUC5AC Expression in Various Tumor Types and Nonneoplastic Tissue: A Tissue Microarray Study on 10 399 Tissue Samples. *Technol. Cancer Res. Treat.* **20**, 15330338211043328 (2021).

22. Singanayagam, A. *et al.* Airway mucins promote immunopathology in virus-exacerbated chronic obstructive pulmonary disease. *J. Clin. Invest.* **132**, (2022).

23. Ambort, D. *et al.* Function of the CysD domain of the gel-forming MUC2 mucin. *Biochem. J.* **436**, 61–70 (2011).

24. Demouveaux, B. *et al.* Mucin CYS domain stiffens the mucus gel hindering bacteria and spermatozoa. *Sci. Rep.* **9**, 16993 (2019).

25. Guo, S. *et al.* Research on the fate of polymeric nanoparticles in the process of the intestinal absorption based on model nanoparticles with various characteristics: size, surface charge and pro-hydrophobics. *J. Nanobiotechnology* **19**, 32 (2021).

26. Popov, A. Mucus-Penetrating Particles and the Role of Ocular Mucus as a Barrier to Micro- and Nanosuspensions. *J. Ocul. Pharmacol. Ther.* **36**, 366–375 (2020).

27. Yu, M. *et al.* Rotation-Facilitated Rapid Transport of Nanorods in Mucosal Tissues. *Nano Lett.* **16**, 7176–7182 (2016).

28. Wu, Y. *et al.* Mushroom-brush transitional conformation of mucus-inert PEG coating improves co-delivery of oral liposome for intestinal metaplasia therapy. *Biomater. Adv.* **136**, 212798 (2022).

29. Yamazoe, E., Fang, J.-Y. & Tahara, K. Oral mucus-penetrating PEGylated liposomes to improve drug absorption: Differences in the interaction mechanisms of a mucoadhesive liposome. *Int. J. Pharm.* **593**, 120148 (2021).

30. Tan, X. *et al.* Hydrophilic and Electroneutral Nanoparticles to Overcome Mucus Trapping and Enhance Oral Delivery of Insulin. *Mol. Pharm.* **17**, 3177–3191 (2020).

31. Zhu, J. *et al.* Surface Coating of Pulmonary siRNA Delivery Vectors Enabling Mucus Penetration, Cell Targeting, and Intracellular Radical Scavenging for Enhanced Acute Lung Injury Therapy. *ACS Appl. Mater. Interfaces* **14**, 5090–5100 (2022).

32. Ensign, L. M., Cone, R. & Hanes, J. Oral drug delivery with polymeric nanoparticles: The gastrointestinal mucus barriers. *Adv. Drug Deliv. Rev.* **64**, 557–570 (2012).

33. Gniewek, P. & Kolinski, A. Coarse-grained Monte Carlo simulations of mucus: structure, dynamics, and thermodynamics. *Biophys. J.* **99**, 3507–3516 (2010).

34. Moreno, N., Perilla, J. E., Colina, C. M. & Lísal, M. Mucin aggregation from a rod-like meso-scale model. *Mol. Phys.* **113**, 898–909 (2015).

35. Flow and aggregation of rod-like proteins in slit and cylindrical pores coated with polymer brushes: an insight from dissipative particle dynamics - Soft Matter (RSC Publishing) DOI:10.1039/C6SM02751B. https://pubs.rsc.org/en/content/articlehtml/2017/sm/c6sm02751b.

36. Ford, A. G. *et al.* Molecular dynamics simulations to explore the structure and rheological properties of normal and hyperconcentrated airway mucus. *Stud. Appl. Math.* **147**, 1369–1387 (2021).

37. Wang, J. & Shi, X. Molecular dynamics simulation of diffusion of nanoparticles in mucus. *Acta Mech. Solida Sin.* **30**, 241–247 (2017).

38. Bao, C. *et al.* Enhanced Transport of Shape and Rigidity-Tuned α-Lactalbumin Nanotubes across Intestinal Mucus and Cellular Barriers. *Nano Lett.* **20**, 1352–1361 (2020).

39. Single-particle diffusional fingerprinting: A machine-learning framework for quantitative analysis of heterogeneous diffusion | PNAS. https://www.pnas.org/doi/10.1073/pnas.2104624118.

40. Capon, C. *et al.* Oligosaccharide structures of mucins secreted by the human colonic cancer cell line CL.16E. *J. Biol. Chem.* **267**, 19248–19257 (1992).

41. Valentine, M. T. *et al.* Colloid Surface Chemistry Critically Affects Multiple Particle Tracking Measurements of Biomaterials. *Biophys. J.* **86**, 4004–4014 (2004).

42. Popielarski, S. R., Hu-Lieskovan, S., French, S. W., Triche, T. J. & Davis, M. E. A nanoparticle-based model delivery system to guide the rational design of gene delivery to the liver. 2. In vitro and in vivo uptake results. *Bioconjug. Chem.* **16**, 1071–1080 (2005).

43. Tarantino, N. *et al.* TNF and IL-1 exhibit distinct ubiquitin requirements for inducing NEMO-IKK supramolecular structures. *J. Cell Biol.* **204**, 231–245 (2014).

44. UniProt: the Universal Protein knowledgebase in 2023. *Nucleic Acids Res.* **51**, D523–D531 (2023).

45. Hughes, G. W. *et al.* The MUC5B mucin polymer is dominated by repeating structural motifs and its topology is regulated by calcium and pH. *Sci. Rep.* **9**, 17350 (2019).

46. Kesimer, M., Makhov, A. M., Griffith, J. D., Verdugo, P. & Sheehan, J. K. Unpacking a gel-forming mucin: a view of MUC5B organization after granular release. *Am. J. Physiol.-Lung Cell. Mol. Physiol.* **298**, L15–L22 (2010).

47. Suvarna, K. S., Layton, C. & Bancroft, J. D. *Bancroft's Theory and Practice of Histological Techniques E-Book*. (Elsevier health sciences, 2018).

48. Desai, M. S. *et al.* A dietary fiber-deprived gut microbiota degrades the colonic mucus barrier and enhances pathogen susceptibility. *Cell* **167**, 1339–1353 (2016).

49. Groot, R. D. & Warren, P. B. Dissipative particle dynamics: Bridging the gap between atomistic and mesoscopic simulation. *J. Chem. Phys.* **107**, 4423–4435 (1997).

50. Luo, Z., Li, Y., Wang, B. & Jiang, J. pH-sensitive vesicles formed by amphiphilic grafted copolymers with tunable membrane permeability for drug loading/release: a multiscale simulation study. *Macromolecules* **49**, 6084–6094 (2016).

51. Hansen, C. M. *Hansen Solubility Parameters: A User's Handbook*. (CRC press, 2007).

52. Ushida, K. & Murata, T. Chapter 4 - Materials Science and Engineering of Mucin: A New Aspect of Mucin Chemistry. in *Studies in Natural Products Chemistry* (ed. Atta-ur-Rahman) vol. 39 115–159 (Elsevier, 2013).

53. Behrens, I., Stenberg, P., Artursson, P. & Kissel, T. Transport of Lipophilic Drug Molecules in a New Mucus-Secreting Cell Culture Model Based on HT29-MTX Cells. *Pharm. Res.* **18**, 1138–1145 (2001).

54. Clark, A. H. & Ross-Murphy, S. B. CHAPTER 1 - Biopolymer Network Assembly: Measurement and Theory. in *Modern Biopolymer Science* (eds. Kasapis, S., Norton, I. T. & Ubbink, J. B.) 1–27 (Academic Press, San Diego, 2009). doi:10.1016/B978-0-12-374195-0.00001-X.

55. Rubinstein, M. & Colby, R. H. *Polymer Physics*. vol. 23 (Oxford university press New York, 2003).

56. Bell, A. E. *et al.* Properties of Gastric and Duodenal Mucus: Effect of Proteolysis, Disulfide Reduction, Bile, Acid, Ethanol, and Hypertonicity on Mucus Gel Structure. *Gastroenterology* **88**, 269–280 (1985).

57. Chaudhuri, O. Viscoelastic hydrogels for 3D cell culture. *Biomater. Sci.* **5**, 1480–1490 (2017).

58. Chaudhuri, O., Cooper-White, J., Janmey, P. A., Mooney, D. J. & Shenoy, V. B. Effects of extracellular matrix viscoelasticity on cellular behaviour. *Nature* **584**, 535–546 (2020).

59. Parrish, E., Caporizzo, M. A. & Composto, R. J. Network confinement and heterogeneity slows nanoparticle diffusion in polymer gels. *J. Chem. Phys.* **146**, 203318 (2017).

60. Lieleg, O. & Ribbeck, K. Biological hydrogels as selective diffusion barriers. *Trends Cell Biol.* **21**, 543–551 (2011).

61. Tsuji, Y., Li, X. & Shibayama, M. Evaluation of mesh size in model polymer networks consisting of tetra-arm and linear poly (ethylene glycol) s. *Gels* **4**, 50 (2018).

62. Moncure, P. J., Simon, Z. C., Millstone, J. E. & Laaser, J. E. Relationship between Gel Mesh and Particle Size in Determining Nanoparticle Diffusion in Hydrogel Nanocomposites. *J. Phys. Chem. B* **126**, 4132–4142 (2022).

63. Bhattacharya, S. & Gubbins, K. E. Fast Method for Computing Pore Size Distributions of Model Materials. *Langmuir* **22**, 7726–7731 (2006).

64. Margulis, C., Stern, H. & Berne, B. Computer simulation of a “green chemistry” room-temperature ionic solvent. *J. Phys. Chem. B* **106**, 12017–12021 (2002).

65. Kob, W. & Andersen, H. C. Testing mode-coupling theory for a supercooled binary Lennard-Jones mixture I: The van Hove correlation function. *Phys. Rev. E* **51**, 4626–4641 (1995).

66. Davis, M. E., Chen, Z. & Shin, D. M. Nanoparticle therapeutics: an emerging treatment modality for cancer. *Nat. Rev. Drug Discov.* **7**, 771–782 (2008).

67. Hickey, J. W., Santos, J. L., Williford, J.-M. & Mao, H.-Q. Control of polymeric nanoparticle size to improve therapeutic delivery. *J. Controlled Release* **219**, 536–547 (2015).

68. Pan, Y. *et al.* Bioadhesive polysaccharide in protein delivery system: chitosan nanoparticles improve the intestinal absorption of insulin in vivo. *Int. J. Pharm.* **249**, 139–147 (2002).

69. Chen, S. B. Dissipative Particle Dynamics Simulation of Nanoparticle Diffusion in a Crosslinked Polymer Network. *J. Phys. Chem. B* **126**, 7184–7191 (2022).

70. Miller, C. C. & Walker, J. The Stokes-Einstein law for diffusion in solution. *Proc. R. Soc. Lond. Ser. Contain. Pap. Math. Phys. Character* **106**, 724–749 (1997).

71. Hopping Diffusion of Nanoparticles in Polymer Matrices | Macromolecules. https://pubs.acs.org/doi/full/10.1021/ma501608x.

72. Round, A. N. *et al.* Heterogeneity and Persistence Length in Human Ocular Mucins. *Biophys. J.* **83**, 1661–1670 (2002).

73. Shuoker, B. *et al.* Sialidases and fucosidases of Akkermansia muciniphila are crucial for growth on mucin and nutrient sharing with mucus-associated gut bacteria. *Nat. Commun.* **14**, 1833 (2023).

74. Zhai, C., Zhou, H., Gao, T., Zhao, L. & Lin, S. Electrostatically Tuned Microdomain Morphology and Phase-Dependent Ion Transport Anisotropy in Single-Ion Conducting Block Copolyelectrolytes. *Macromolecules* **51**, 4471–4483 (2018).

75. Zhu, B., He, Z., Jiang, G. & Ning, F. Molecular design of switchable nanochannels modified by zwitterion polymer chains with dissipative particle dynamics simulation. *Polymer* **290**, 126602 (2024).